ADVANCES IN NUCLEAR SCIENCE AND APPLICATIONS

Volume 2, No. 2 (2026), P. 139-153

Microstructure of Gd-doped dysprosium hafnate after irradiation with light and heavy ions

M.S. Staltsov[1,*], D.P. Shornikov[1], M.D. Prokhorova[1], S.V. Chuvikov[2], A.A. Urusov[2], A.A. Mokrushin[2], and V.D. Risovaniy[2]

[1]National Research Nuclear University MEPhI, Moscow, Russia

[2]JSC Research Institute NPO Luch, Podolsk, Moscow Region, Russia

e-mail: m.staltsov@gmail.com

DOI: 10.63907/ansa.v2i2.87
Received: 24 May 2026

Abstract

The evolution of the microstructure of the $0.45Dy_2O_3{\cdot}0.50HfO_2{\cdot}0.05Gd_2O_3$ ceramic compound under sequential irradiation with nickel and helium ions is presented. Irradiation was performed at temperatures of 350 and 550 °C to damage doses in the range of 20–300 displacements per atom (dpa). The formation of a shallow and relatively uniform porous layer along the ion penetration path is shown. The average size and number density of voids and helium bubbles increase with increasing irradiation dose and temperature. The highest swelling was observed for the samples irradiated at 550 °C to a dose of 300 dpa. It is shown that Gd-doped dysprosium hafnate exhibits slightly lower porosity and swelling parameters compared with undoped dysprosium hafnate. However, the selected gadolinium content does not allow any explicit trends to be established unambiguously.

1 Introduction

At present, the increase in power output of nuclear power plants is closely related to higher fuel burnup, longer fuel cycles, the capability of operating under load-following conditions, and the reduction in the cost of fuel and core structural materials. At the same time, the requirements for the reliable and safe operation of both existing and newly constructed power units are becoming increasingly stringent.

To improve reactor safety under all operating conditions, it is necessary to increase the service life of the absorber rods used in the control and protection system. Boron carbide enriched with the $^{10}\mathrm{B}$ isotope is a traditional absorber material characterized by a high neutron absorption efficiency. However, during operation, a considerable amount of helium accumulates in the control element as a result of the $^{10}\mathrm{B}\,(n,\alpha)$ reaction. This helium accumulation may lead to swelling, degradation of the absorber material, and cracking of the cladding. Another disadvantage of B_4C is the burnup of the $^{10}\mathrm{B}$ isotope, which causes a decrease in absorption efficiency after 2–3 years of operation.

Several approaches are being considered as alternatives to boron carbide:

1. the use of composite absorbers based on mixtures of boron carbide with other absorber materials, such as dysprosium titanate or dysprosium hafnate;
2. the use of boron-free absorber materials, including dysprosium hafnate, dysprosium titanate, hafnium hydride, and Ag–In–Cd alloys;
3. the use of composite absorbers based on dysprosium hafnate with additional absorbing elements, such as gadolinium or erbium oxides.

It should be noted that boron-free absorber materials are generally characterized by a lower absorption efficiency, approximately 75–85% of that of boron carbide used as a reference material. However, these compounds do not exhibit the main disadvantages typical of boron carbide, namely swelling and cracking caused by helium accumulation. In addition, dysprosium hafnate can retain its absorption capacity over long-term operation due to the formation of isotopes with high neutron absorption ability in the chain of nuclear transformations.

For Russian VVER-type reactors, the use of two types of absorber rods is considered promising: rods based on boron carbide and rods based on dysprosium hafnate. In this concept, emergency protection (EP) rods containing boron carbide are used for reactor shutdown, whereas automatic control (AC) rods based on dysprosium hafnate are used for automatic core power control. The use of such AC rods also makes it possible to reduce the role of boric acid as an auxiliary absorber in the primary coolant.

The lower part of the AC rod is filled with dysprosium hafnate Dy_2HfO_5, which is exposed to the most intense neutron flux because it remains continuously inside the reactor core. Dysprosium hafnate has a higher radiation resistance than B_4C and does not produce gaseous transmutation products during neutron capture, since neutron absorption proceeds mainly via the (n,γ) reaction [1–4]. In addition, the broad solid-solution region in the $HfO_2-Dy_2O_3$ system over a wide range of molar concentrations makes it possible to stabilize dysprosium hafnate with a cubic fluorite-type structure, which is known to exhibit enhanced radiation resistance [5,6].

The presence of two absorbing elements, Dy and Hf, increases the neutron-physical efficiency of dysprosium hafnate to approximately 80–90% of that of reference B_4C. One possible approach to increasing this efficiency to nearly 100% is the introduction of gadolinium oxide into Dy_2HfO_5. Gadolinium oxide has long been widely used as a burnable absorber in VVER fuel pellets. Neutronic calculations show that the addition of up to 5 mol.% gadolinium oxide increases the absorption capacity of dysprosium hafnate by 2–5%, which can generally be considered sufficient for reliable operation of the control element. Moreover, the introduction of gadolinium oxide does not change the fluorite lattice of dysprosium hafnate and does not reduce the radiation resistance of the compound [1, 5].

At the same time, there is still little experimental evidence in the literature to confirm these assumptions. The available data on the radiation resistance of pure dysprosium hafnate are contradictory, which may be largely associated with differences in the fabrication conditions of Dy_2HfO_5. These differences can prevent the formation of an ideal solid solution and, consequently, the stabilization of a single fluorite structure. Data on the effect of gadolinium additives on the radiation resistance of dysprosium hafnate are also practically absent. Therefore, the investigation of the effect of ion irradiation on gadolinium-doped Dy_2HfO_5 is a relevant and timely research task.

2 Materials and Methods

Samples of Gd-doped dysprosium hafnate with the composition $0.45Dy_2O_3{\cdot}0.50HfO_2{\cdot}0.05Gd_2O_3$ were studied. The fabrication procedure is described in detail in [4]. The samples were sequentially irradiated with Ni^{4+} ions with an energy of 11.5 MeV and He^{+} ions with energies of 0.8 and 1.4 MeV. The damage dose at the peak of the heavy-ion irradiation profile was varied in the range of 20–300 displacements per atom (dpa). The helium implantation level corresponded to 84 appm He/dpa. The main irradiation parameters, including temperature and damage dose, are listed in Table 1.

Table 1: Irradiation conditions for dysprosium hafnate samples.

Sample	Temperature, °C	Damage dose, dpa
$0.45Dy_2O_3 \cdot 0.50HfO_2 \cdot 0.05Gd_2O_3$		
1	350	20
2	350	100
3	350	200
4	350	300
5	550	20
6	550	100
7	550	200
8	550	300

The results of SRIM-2013 calculations of ion ranges and damage dose profiles as a function of sample depth are also presented in [4]. According to these calculations, the maximum concentrations of implanted Ni, He (0.8 MeV), and He (1.4 MeV) ions are located at depths of approximately 3.8, 1.9, and 3.0 μm, respectively. The maximum number of displacements per atom is observed at a depth of about 3.5 μm. Based on these data, the microstructure of the irradiated samples was examined to a depth of approximately 2 μm, where TEM-resolvable porosity is mainly formed in the region of overlapping helium accumulation and displacement damage. The microstructure and elemental composition of the sample cross sections were studied using a Tecnai G2 F20 transmission electron microscope (FEI, the Netherlands) with a spatial resolution of 0.24 nm in transmission electron microscopy (TEM) mode and 0.10 nm in scanning transmission electron microscopy (STEM) mode. Images used for porosity analysis were obtained in bright-field TEM mode using Fresnel contrast. Elemental maps and elemental distribution profiles were obtained in high-angle annular dark-field STEM (HAADF-STEM) mode, which provides atomic-number contrast. During the porosity analysis, pairs of bright-field images were obtained for each examined region under underfocus and overfocus conditions. In the calculation of porosity parameters, features that changed their contrast upon passing through the focus were identified as voids or helium bubbles. The elemental composition of the samples was analyzed by energy-dispersive X-ray spectroscopy (EDS) using an EDAX Apollo energy-dispersive spectrometer (AMETEK, USA) with an energy resolution of 125 eV and a detection sensitivity of 0.1 wt.%. The spectrometer was coupled with the Tecnai G2 F20 transmission electron microscope.

3 Experimental Results

Figure 1a shows the microstructure of the near-surface layer of sample 1 irradiated to a damage dose of 20 dpa at 350 °C. The red dashed line indicates the sample surface.

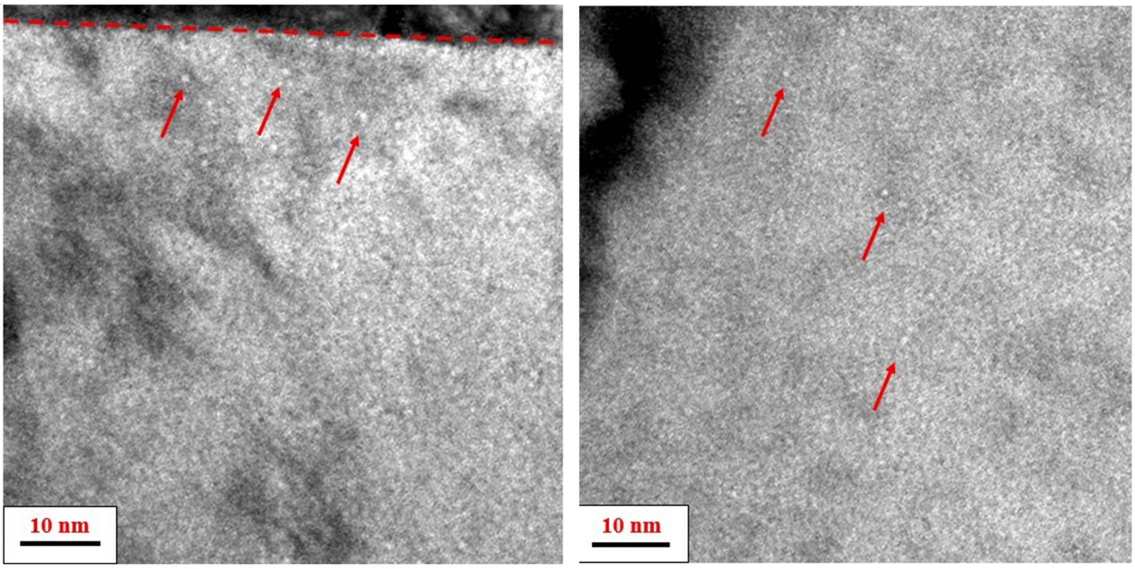

(a) (b)

Figure 1: Microstructure of sample 1 irradiated to a damage dose of 20 dpa at 350 °C at depths of (a) ∼0–70 nm and (b) ∼350–420 nm.

Individual features identified as voids/bubbles were observed in the subsurface layer of sample 1, as indicated by arrows in Figure 1a. The maximum diameter of these voids/bubbles was approximately 1–1.5 nm. Since the size of the observed features is close to the spatial resolution limit of the TEM images, accurate determination of their dimensions is difficult. According to the microstructural observations at a depth of approximately 400 nm, the size and spatial distribution of voids/bubbles do not change significantly with depth. Voids/bubbles with a similar diameter of approximately 1–1.5 nm were observed and were sparsely distributed in the matrix, as indicated by arrows in Figure 1b. The identification of porosity in deeper layers of sample 1 was limited by the absence of clearly visible defects and by the very small size of the observed features. Due to the extremely small size and low number density of voids/bubbles in sample 1, the average swelling over the irradiated region was estimated to be approximately 0.01% (Table 2). The microstructure of the subsurface layer of sample 2 is shown in Figure 2. Small voids/bubbles with a diameter of approximately 1–1.5 nm were formed in the near-surface region. In some areas, clusters or chains of voids/bubbles were also observed, as marked by boxes in Figure 2a. The number density of voids/bubbles slightly increased compared with sample 1 (Table 2). A similar defect morphology was observed in deeper regions of the hafnate matrix. For example, Figure 2b shows the microstructure of the region at a depth of approximately 900 nm.

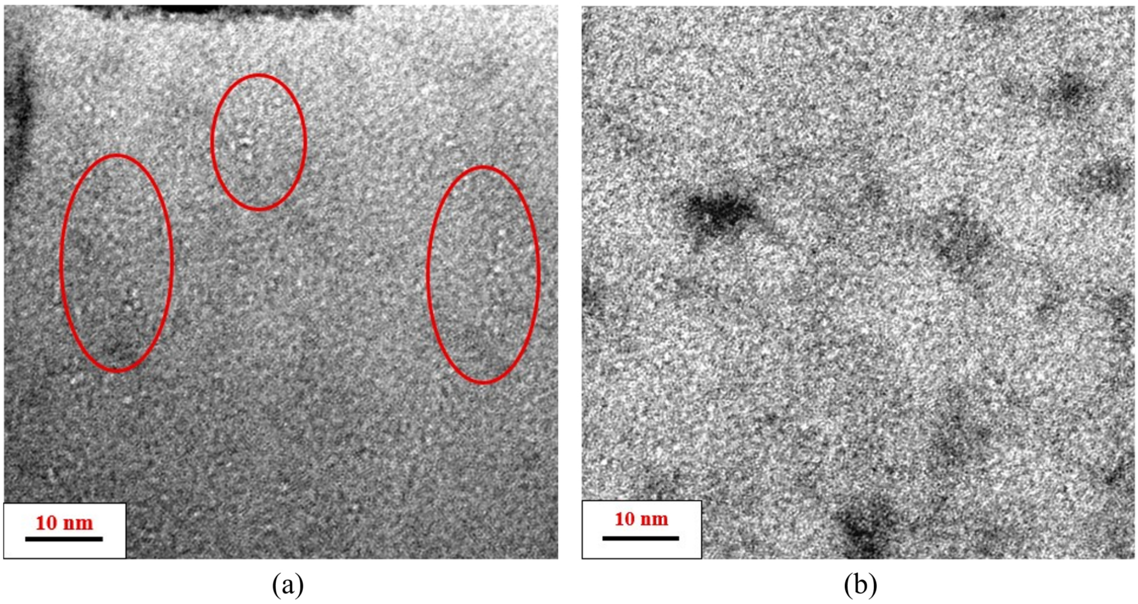

(a) (b)

Figure 2: Microstructure of sample 2 irradiated to a damage dose of 100 dpa at 350 °C: (a) depth of ∼0–70 nm; (b) depth of ∼875–940 nm.

A relatively high number density of features identified as voids/bubbles, with a size not exceeding approximately 1–1.5 nm, was observed. Similar porosity parameters, without any pronounced tendency to decrease with depth, were detected down to a depth of approximately 1700 nm. Due to the higher number density of voids/bubbles, the total swelling of sample 2 increased compared with that of sample 1 irradiated to 20 dpa and reached approximately 0.04%. Figure 3 shows the depth distribution of the main elements and implanted nickel in sample 3 irradiated to 200 dpa. As can be seen, the maximum nickel concentration is observed at a depth of approximately 2.8 μm. The intensity of this maximum increases with irradiation dose, which is consistent with the results reported in [4]. Similar elemental distributions were observed for the other samples; however, the amount of implanted nickel increased with increasing dose.

The results of the high-resolution microstructural analysis of the near-surface layer of sample 3 irradiated to a damage dose of 200 dpa at 350 °C are shown in Figure 4a. Individual voids/bubbles with a maximum size not exceeding approximately 1 nm

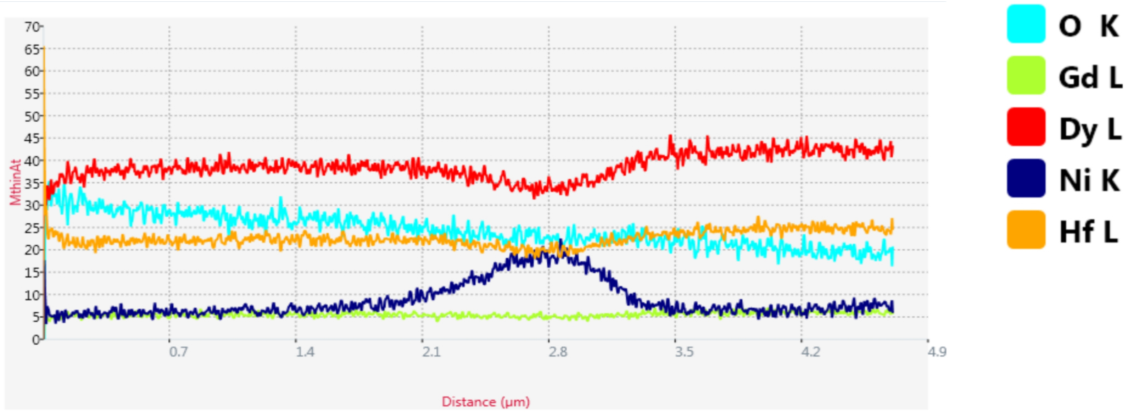

Figure 3: Depth distribution of the main elements and implanted nickel in sample 3 after irradiation to 200 dpa at 350 ° C.

were observed directly in the subsurface layer. Small chains of voids/bubbles were also detected, as marked by frames in Figure 4a. Similar voids/bubbles were observed throughout the irradiated layer (Figure 4b); however, their number density was higher than in the subsurface region.

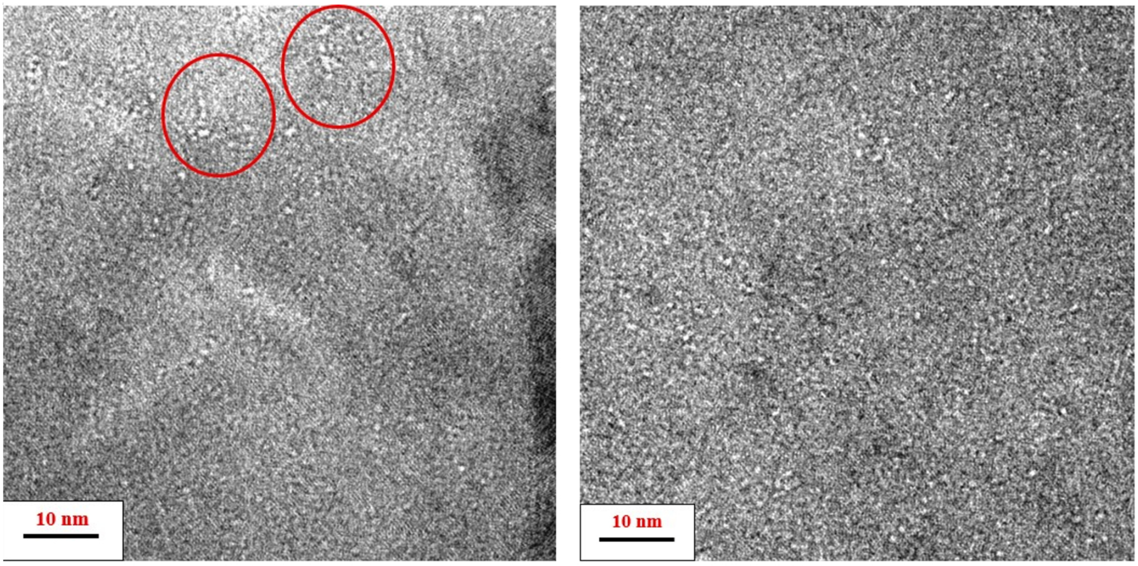

(a) (b)

Figure 4: Microstructure of sample 3 irradiated to a damage dose of 200 dpa at 350 ° C: (a) depth of ∼0–70 nm; (b) depth of ∼1170–1240 nm.

Based on the microstructural analysis of sample 3 (Figure 4), it can be concluded that the microstructure changes only slightly with depth. The porosity parameters averaged over the entire irradiated layer are presented in Table 2. As follows from the table, the swelling increased slightly compared with sample 2 irradiated to 100 dpa and reached approximately 0.05%, mainly due to a slight increase in the number density of voids/bubbles. Figure 5a shows a high-resolution image of the subsurface microstructure of sample 4. As can be seen, voids/bubbles with a size of approximately 1–1.5 nm are uniformly distributed in the near-surface layer of the sample and are characterized by a relatively high number density. With increasing distance from the sample surface, no significant changes in the porosity parameters were observed. Voids/bubbles with a high number density and a maximum size not exceeding approximately 1–1.5 nm were detected throughout the irradiated layer. At larger distances from the surface, the size of the voids/bubbles appears to decrease slightly. For example, Figure 5b shows the microstructure of a region located at a depth of approximately 1400 nm. According to Table 2, the calculated swelling of the irradiated layer in sample 4 was the highest among all samples irradiated at 350 °C and amounted to approximately $0.10 \pm 0.02\,\%$.

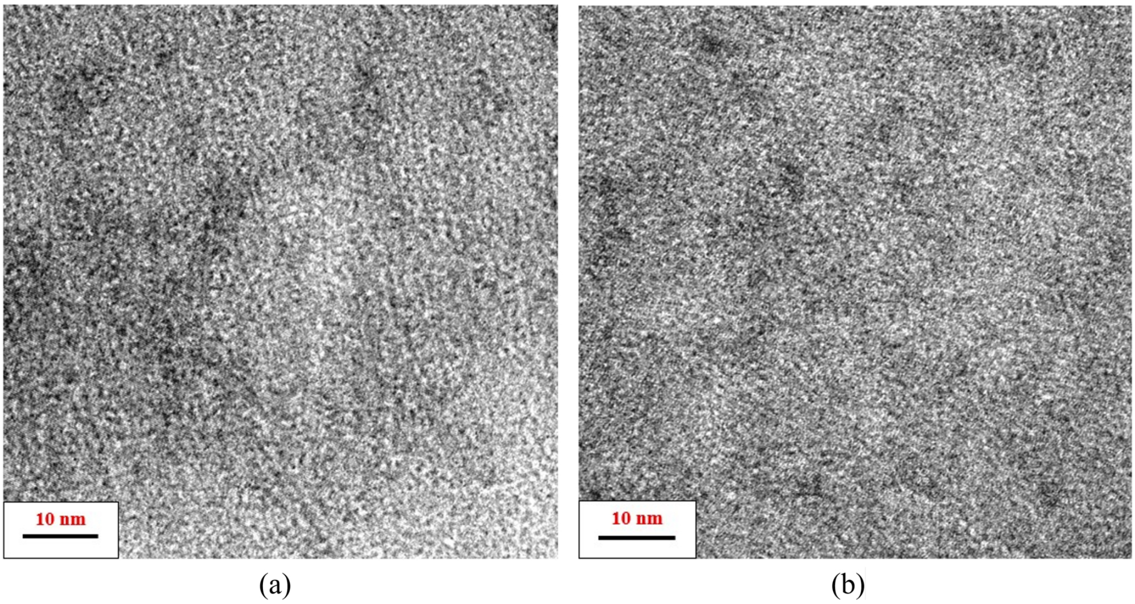

(a) (b)

Figure 5: Microstructure of sample 4 irradiated to 300 dpa at 350 °C: (a) ~0–70 nm; (b) ~1355–1425 nm.

Figure 6a shows the microstructure of the subsurface layer of sample 5 irradiated to a damage dose of 20 dpa at 550 °C. Features identified as voids/bubbles with an average size of approximately 1 nm were observed. Individual voids/bubbles with sizes reaching approximately 1.5 nm were also detected. It can be seen that the voids/bubbles often form clusters or chains, as marked by boxes in Figure 6a.

The formation of such clusters in the near-surface region may be associated with the enhanced mobility of radiation-induced point defects and helium at 550 °C. Although the damage dose for sample 5 was relatively low, the increased irradiation temperature apparently promotes the migration and coalescence of helium-vacancy complexes, leading to the local grouping of small voids/bubbles. At the same time, the small size of the observed features indicates that the porosity remains at an early stage of development. With increasing distance from the surface, the tendency toward the formation of clusters or chains of voids/bubbles becomes less pronounced. The voids/bubbles are rather uniformly distributed in the material matrix. For example,

Figure 6b shows the microstructure of a region located at a distance of approximately 1 μm from the surface. As can be seen, the average void/bubble size is in the range of approximately 1–1.5 nm. Thus, irradiation at 550 °C to 20 dpa results in the formation of a fine and relatively uniform porous structure throughout the analyzed irradiated layer. Compared with the samples irradiated at 350 °C to the same dose, the higher irradiation temperature is expected to increase defect mobility and facilitate the formation of a more developed void/bubble structure, even at the initial damage level.

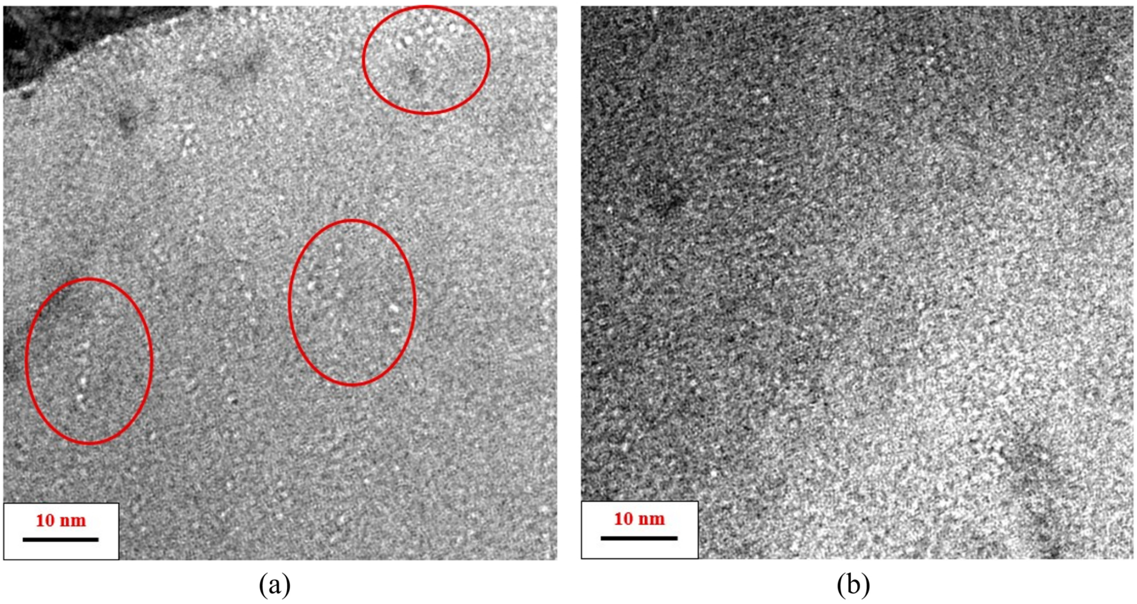

Figure 6: Microstructure of sample 5 irradiated to a damage dose of 20 dpa at 550 ° C: (a) depth of ∼0–70 nm; (b) depth of ∼975–1040 nm.

The porosity analysis of sample 5 showed that the average swelling of the irradiated layer over the entire analyzed depth was approximately 0.05% (Table 2). The observed porosity demonstrates that, even at the lowest damage dose, irradiation at 550 ° C promotes the formation of a developed population of nanosized voids/bubbles. Therefore, the subsequent samples irradiated at the same temperature were analyzed to clarify the dose dependence of porosity formation.

Figure 7a shows the microstructure of the near-surface layer of sample 6 irradiated to a damage dose of 100 dpa at 550 ° C. Features that can be identified as voids/bubbles were observed directly near the surface and often formed clusters or chains, some of which are marked by frames in Figure 7a. The size of most voids/bubbles was in the range of approximately 1–1.5 nm, and their number density was relatively high. The diameter of the largest voids/bubbles reached approximately 2 nm. With increasing distance from the sample surface, the tendency toward chain formation became less pronounced, and the voids/bubbles were distributed more uniformly within the grain interior. For example, Figure 7b shows the microstructure of a region located at a depth of approximately 900 nm from the surface. The average size of the features at this depth remained approximately the same as in the near-surface layer; however, voids/bubbles with sizes up to 2 nm, observed near the surface, were not detected. The average porosity parameters are presented in Table 2. The total swelling of the irradiated layer in sample 6 was approximately 0.05%, which, within the experimental uncertainty, coincides with the swelling of sample 5 irradiated to 20 dpa. The microstructure of the near-surface layer of sample 7 irradiated to a damage dose of 200 dpa at 550 ° C is shown in Figure 8a. Voids/bubbles up to approximately 2 nm in size were detected and locally formed chains or clusters, as outlined in Figure 8a. With increasing distance from the surface, the chains of voids/bubbles gradually disappeared, and the void/bubble size did not exceed approximately 1.5 nm.

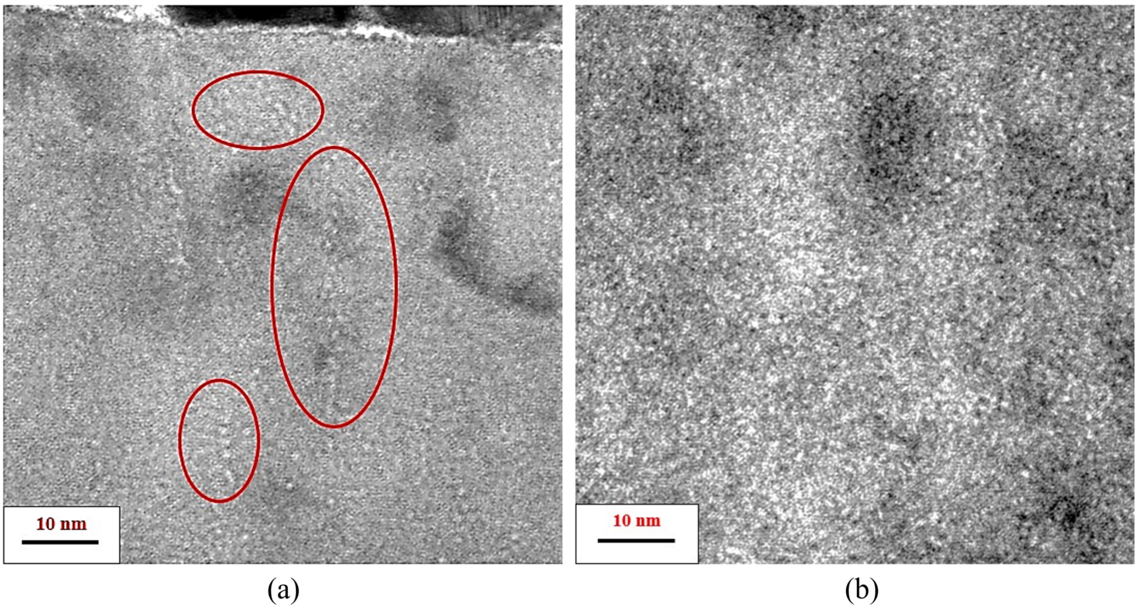

(a) (b)

Figure 7: Microstructure of sample 6 irradiated to a damage dose of 100 dpa at 550 ° C: (a) depth of ∼0–70 nm; (b) depth of ∼850–920 nm.

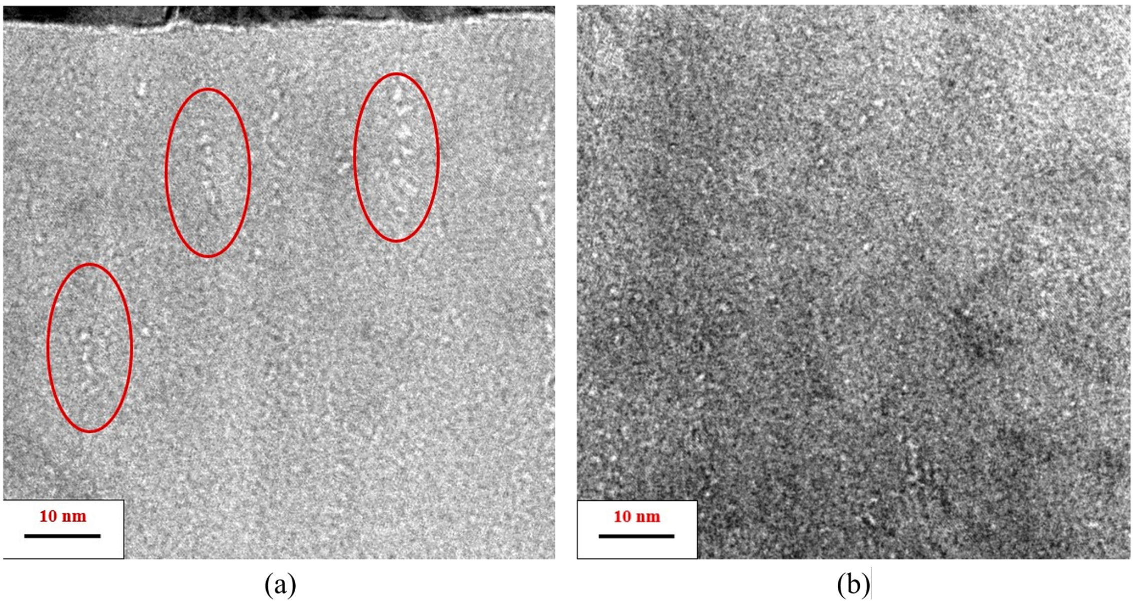

(a) (b)

Figure 8: Microstructure of sample 7 irradiated to a damage dose of 200 dpa at 550 ° C: (a) depth of ∼0–70 nm; (b) depth of ∼210–285 nm.

The microstructural analysis of regions located farther from the surface showed an increase in the porosity parameters. Figure 9a shows the microstructure of a region located at a depth of approximately 600 nm. In this region, the void/bubble size visually increased, whereas their number density changed only slightly. The maximum void/bubble size reached approximately 2.5 nm; several such features are highlighted in Figure 9a.

Studies of deeper material layers showed that similar sizes and number densities of voids/bubbles were retained down to the maximum analyzed depth. Figure 9b shows the microstructure of a region located at a depth of approximately 1200 nm from the surface. No noticeable changes in the porosity parameters were observed up to the end of the analyzed layer in sample 7.

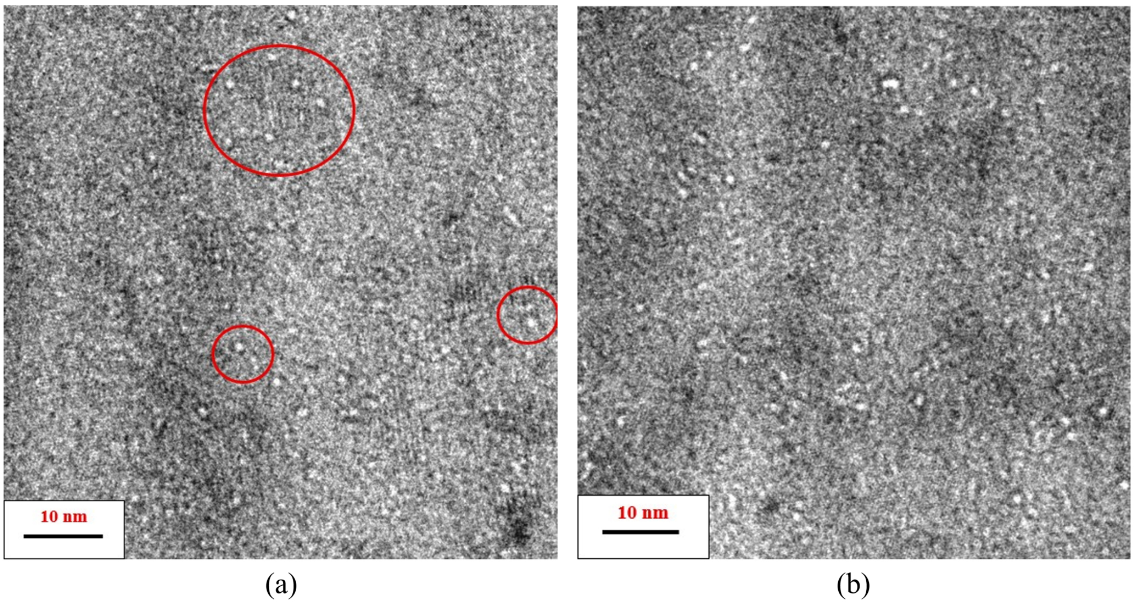

(a) (b)

Figure 9: Microstructure of sample 7 irradiated to a damage dose of 200 dpa at 550 °C: (a) depth of ∼575–650 nm; (b) depth of ∼1175–1235 nm.

The porosity parameters averaged over the entire irradiated layer indicate that swelling increased by nearly a factor of two compared with sample 6 irradiated to 100 dpa. Nevertheless, the swelling of sample 7 did not exceed approximately 0.1%, which indicates a relatively low degree of radiation- induced volumetric degradation under these irradiation conditions.

Figure 10a shows the microstructure of sample 8 irradiated to a damage dose of 300 dpa at 550 °C. The analyzed region was located at a distance of approximately 100 nm from the surface. Rather uniformly distributed voids/bubbles with sizes of approximately 1–1.5 nm were observed.

With increasing distance from the surface, the number density and size of voids/bubbles increased slightly. Thus, Figure 10b shows a more developed porous structure in sample 8 at a depth of approximately 1000 nm. The voids/bubbles were more densely distributed than in the near-surface layer, and some of them reached approximately 2 nm in size. The swelling increased slightly to approximately 0.12%, apparently due to the more pronounced porosity in the deeper region of the irradiated layer.

Specific microstructural features were observed in the samples irradiated to high damage doses of 200 and 300 dpa. A relatively developed porous structure was detected at larger depths. Figure 11 shows the microstructures of samples 7 and 8 at distances of approximately 1600 and 1750 nm from the surface, respectively. A rather high number density of voids/bubbles was observed in these regions (Table 2), and their maximum size reached approximately 2 nm.

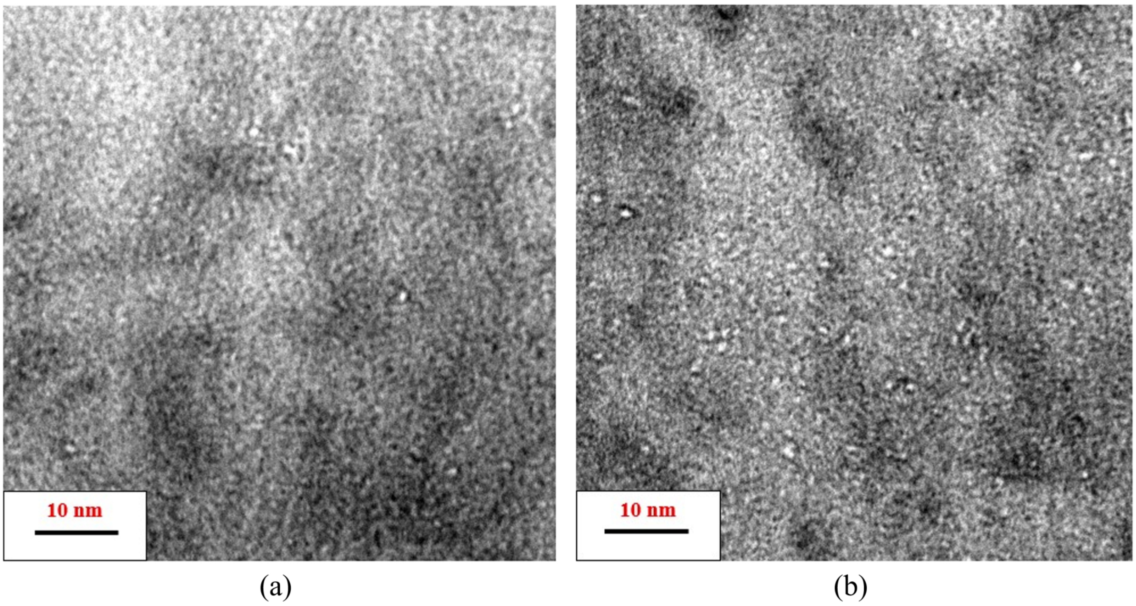

Figure 10: Microstructure of sample 8 irradiated to a damage dose of 300 dpa at 550 °C at distances from the surface of (a) ∼90–180 nm and (b) ∼1150–1240 nm.

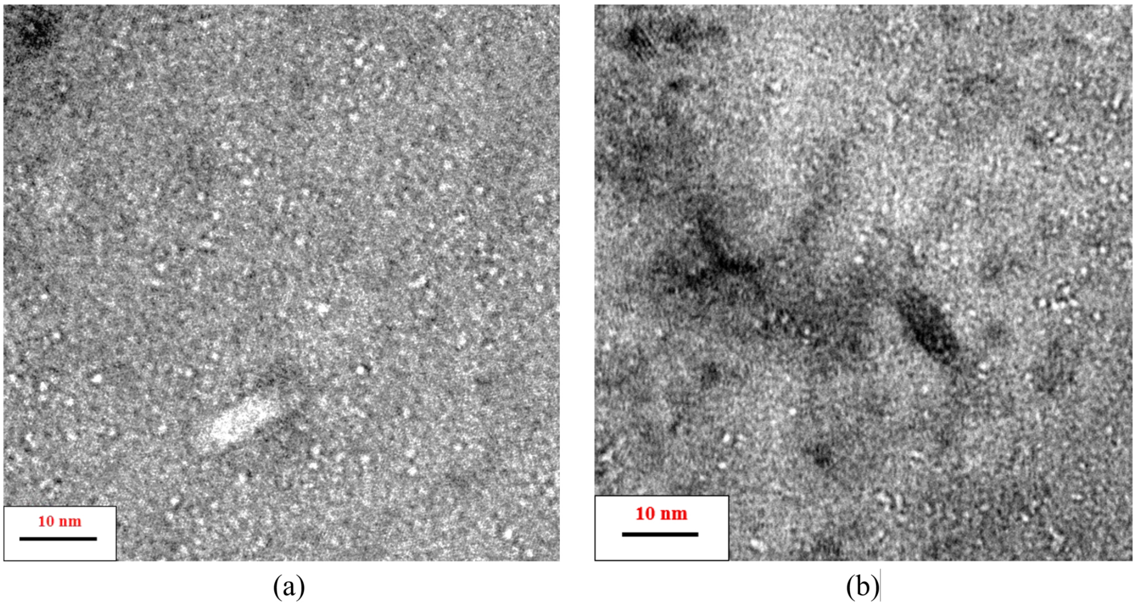

Figure 11: Microstructure of the deep irradiated regions: (a) sample 7 irradiated to 200 dpa at 550 °C at a depth of ∼1570–1650 nm; (b) sample 8 irradiated to 300 dpa at 550 °C at a depth of ∼1700–1790 nm.

4 Discussion

The porosity and swelling parameters determined from the TEM micrographs of the $0.45Dy_2O_3 \cdot 0.50HfO_2 \cdot 0.05Gd_2O_3$ ceramic compound after sequential irradiation with nickel and helium ions are summarized in Table 2. Analysis of Figures 1–11 and the data presented in Table 2 shows that the average size of the detected gas-filled voids/bubbles in all samples lies within a narrow range of approximately 1.3–1.7 nm. At the same time, the maximum void/bubble size slightly increases with increasing damage dose and reaches approximately 2.5 nm in sample 8. The number density of voids/bubbles also increases with irradiation temperature and damage dose. This results in a slight increase in swelling of the irradiated layer. Nevertheless, the swelling remains very low, as was also observed for dysprosium hafnate samples without gadolinium modification [4]. Low swelling of ceramic materials at these temperatures is not unusual. It has been shown repeatedly that pronounced swelling in ceramics can occur either at relatively low or at high temperatures, depending on the dominant defect-evolution mechanisms [7–11]. The irradiation temperatures used in the present experiment fall within the temperature range in which swelling is expected to remain sufficiently low.

Table 2: Porosity parameters and calculated swelling values of $0.45\mathrm{Dy_2O_3} \cdot 0.50\mathrm{HfO_2} \cdot 0.05\mathrm{Gd_2O_3}$ samples irradiated to various damage doses at temperatures of 350 and 550 °C.

Sample	Dose, dpa	Temperature, °C	d, nm	Number density, $\mathrm{m^{-3}}$	Swelling, %
1	20	350	1.5 ± 0.3	$(6.4 \pm 0.1) \times 10^{22}$	0.013 ± 0.003
2	100	350	1.4 ± 0.3	$(2.4 \pm 0.4) \times 10^{23}$	0.04 ± 0.01
3	200	350	1.3 ± 0.3	$(4.0 \pm 0.8) \times 10^{23}$	0.05 ± 0.01
4	300	350	1.5 ± 0.3	$(5.6 \pm 1.1) \times 10^{23}$	0.10 ± 0.02
5	20	550	1.4 ± 0.3	$(2.9 \pm 0.6) \times 10^{23}$	0.05 ± 0.01
6	100	550	1.5 ± 0.4	$(3.0 \pm 0.6) \times 10^{23}$	0.05 ± 0.01
7	200	550	1.7 ± 0.6	$(3.1 \pm 0.6) \times 10^{23}$	0.10 ± 0.05
8	300	550	1.7 ± 0.5	$(3.3 \pm 0.6) \times 10^{23}$	0.12 ± 0.05

Special attention should be paid to the formation of voids/bubbles at relatively large depths in samples 7 and 8 irradiated to high damage doses at 550 °C. At damage doses of 200 and 300 dpa, the concentrations of excess vacancies and helium in the deeper regions of the irradiated layer apparently become sufficiently high for void/bubble formation at elevated temperature (Figure 11). At lower doses or lower temperatures, the void/bubble size at depths of 1.5–2 μm decreased, which may indicate that the effective maximum of vacancy accumulation and porosity development in the studied samples was shifted toward a depth of approximately 1 μm.

The assessment of the actual damage distribution in irradiated materials, including calculations using the SRIM software package, remains an important problem in radiation materials science. It has been shown that such calculation tools may overestimate both the damage level and the spatial extent of the damage profile [12]. In the present case, the complex structure of the ceramic compound, the specific features of defect, helium, and implanted nickel redistribution in the ceramic lattice, as well as the relatively low irradiation temperature for ceramics, may lead to a noticeable shift between the calculated and experimentally observed regions of maximum porosity development. Under high-dose irradiation, the maximum void/bubble size and swelling were observed at a depth of approximately 1000 nm; however, the size of voids/bubbles located in deeper regions also remained significant.

Comparison of the present results with those reported in [4] shows that there are no substantial differences between Gd-doped and undoped dysprosium hafnate. The size and number density of voids/bubbles are comparable, as are the swelling values of the irradiated layer. The general pattern of porosity development is also very similar.

Chains of voids/bubbles were often observed in the subsurface layer. Their formation may be associated with ion tracks. In general, the formation of tracks, including latent tracks, during ion irradiation of ceramics is a well-known phenomenon [13–16]. It is usually related to local structural transformations, such as allotropic transformations, local amorphization, or recrystallization, occurring along the trajectory of a high-energy ion passing through the crystal lattice. Such tracks are most often observed in subsurface layers, where the ion energy remains high. In the present case, high-energy nickel ions can apparently induce local overheating in the dysprosium hafnate lattice and produce regions of local structural transformation and elastic stress. Such regions may act as preferential nucleation sites for voids/bubbles [17,18]. Since sequential irradiation was used in the present experiment, chains of voids/bubbles could form in these locally modified regions. Similar effects have been reported, for example, for ceramics irradiated with high-energy noble gas ions [14].

Chains of bubbles were also observed in the reference experiment [4]. This interpretation is supported by the fact that bubble chains were formed mainly in the subsurface layer and that their direction coincided with the ion-beam direction. Thus, in the near-surface region, the ions still have sufficient energy to induce local overheating and/or a high degree of atomic displacement. In deeper layers of the material, their energy is apparently insufficient to produce similar track-related defect structures.

Overall, the analysis of porosity and swelling in Gd-doped dysprosium hafnate indicates that gadolinium has no pronounced effect on microstructure evolution under simulated irradiation with nickel and helium ions. It may even be concluded that, on average, the void/bubble size is slightly smaller than in dysprosium hafnate without gadolinium. This effect may be associated with the formation of more stable helium-vacancy complexes upon doping, as well as with the presence of additional elements in the solid solution and the formation of additional void/bubble nucleation sites at lattice distortions. Similar effects have been reported for metals and alloys [17,18]. However, since the characteristic size of the observed features is only 1–2 nm, any trend should be interpreted with caution. The object sizes are close to the resolution limit of the microscope and often coincide within the experimental uncertainty.

Summarizing the comparison between undoped dysprosium hafnate [4] and Gd-doped dysprosium hafnate studied in the present work, it can be concluded that dysprosium hafnate exhibits high resistance to void and gas swelling at the irradiation temperatures used, even up to high damage doses. This behavior can be explained by the relatively low homologous temperature of the experiment. The maximum swelling of approximately 0.1% was detected in the samples irradiated to the highest doses (Table 2). Such a swelling level is extremely low for reactor materials [7,19] and is unlikely to be a limiting factor for the operability of absorber elements under reactor conditions.

The results of [4] concerning the absence of amorphization in ceramic dysprosium hafnate under irradiation are also confirmed. Under the present experimental conditions, gadolinium addition does not lead to amorphization of the samples.

5 Conclusions

Based on the results of the microstructural study of the $0.45Dy_2O_3 \cdot 0.50HfO_2 \cdot 0.05Gd_2O_3$ ceramic compound after sequential irradiation with 11.5 MeV nickel ions and helium ions with energies of 0.8 and 1.4 MeV to damage doses of 20–300 dpa at temperatures of 350 and 550 °C, the following conclusions can be drawn:

1. Under the irradiation conditions used in this work, fine porosity was formed in the structure of Gd-doped dysprosium hafnate. The maximum size of voids/bubbles reached approximately 2.5 nm. The void/bubble size and number density generally increased with increasing irradiation temperature and damage dose.

2. Gadolinium doping of dysprosium hafnate did not significantly affect the porosity and swelling parameters compared with undoped dysprosium hafnate. Nevertheless, a slight tendency toward lower void/bubble size and swelling can be distinguished.

3. The maximum swelling of the irradiated layer was observed in the samples irradiated to 300 dpa at 350 and 550 °C. The highest swelling value was approximately 0.12%, which remains very low for reactor materials.

4. No amorphization of the ceramic structure was detected under the irradiation temperatures and damage doses used in this study.

5. The studied Gd-doped dysprosium hafnate ceramic demonstrates high resistance to void and gas swelling under irradiation conditions simulating long-term operation of absorber materials in VVER-type reactors.

References

[1] V. Risovaniy *et al.*, Dysprosium in Nuclear Engineering (Dimitrovgrad, 2011), 222 p. (In Russian).

[2] A. Zakharov *et al.*, Proc. IX Russian Conf. Reactor Materials Science, Dimitrovgrad, 366 (2009) (In Russian).

[3] V. Risovaniy *et al.*, VANT, Ser. Physics of Radiation Damage, **3**, 87 (2005) (In Russian).

[4] M. Staltsov *et al.*, Adv. Nucl. Sci. App. **2**, 61 (2026).

[5] V. Risovaniy *et al.*, J. Nucl. Mater. **365**, 163 (2006).

[6] E. B. Perova *et al.*, Izv. Akad. Nauk SSSR, Inorg. Mater. **8**, 1878 (1972) (In Russian).

[7] P. Yvon, Structural Materials for Generation IV Nuclear Reactors (Woodhead Publishing, London, 2017), 664 p.

[8] P. Seo *et al.*, J. Appl. Phys. **132**, 235902 (2022).

[9] J.-M. Costantini *et al.*, J. Nucl. Mater. **564**, 153667 (2022).

[10] Y. Katoh *et al.*, J. Nucl. Mater. **448**, 448 (2014).

[11] X. Su *et al.*, J. Eur. Ceram. Soc. **46**, 118167 (2026).

[12] F. A. Garner, J. Nucl. Mater. **117**, 177 (1983).

[13] J. H. O'Connell *et al.*, Nucl. Instrum. Methods Phys. Res. B **473**, 1 (2020).

[14] S. A. Chyzganov *et al.*, Ceram. Int. **49**, 37061 (2023).

[15] P. P. Hu *et al.*, Nucl. Instrum. Methods Phys. Res. B **568**, 165855 (2025).

[16] A. Kamarou *et al.*, Phys. Rev. B **73**, 184107 (2006).

[17] I. Chernov *et al.*, J. Nucl. Mater. **459**, 259 (2015).

[18] M. Staltsov *et al.*, J. Nucl. Mater. **461**, 54 (2015).

[19] R. J. M. Konings, Comprehensive Nuclear Materials (Elsevier, 2012).